



# Imaging of structure at and near the core mantle boundary using a generalized radon transform:

## 1. Construction of image gathers

P. Wang,<sup>1</sup> M. V. de Hoop,<sup>2</sup> R. D. van der Hilst,<sup>1</sup> P. Ma,<sup>3</sup> and L. Tenorio<sup>4</sup>

Received 22 December 2005; revised 1 July 2006; accepted 21 August 2006; published 15 December 2006.

[1] We introduce a method for imaging heterogeneity at and near interfaces in Earth's lowermost mantle with broadband, three-component seismograms from global seismograph networks. Our approach is based on inverse scattering and allows the extraction of pertinent signal from large data sets and requires few a priori assumptions about the heterogeneity under study, which makes it complementary to the forward modeling of selected waveforms. Here we construct a generalized radon transform (for heterogeneous, anisotropic elastic media) to map broadband seismogram windows, comprising main arrivals with their coda and precursors, into multiple images of a target structure. The "common image point gathers" thus produced reveal multiscale variations in elastic properties near deep interfaces. The GRT can be applied to narrow and wide-angle data, and the (automated) extraction of signal from data over a wide range of epicentral distances enables exploration of core-mantle boundary (CMB) regions that cannot, with present-day data coverage, be imaged with the triplicated waveforms used in forward modeling studies. Tests with synthetic data, produced both with idealized and actual source-receiver distributions, illustrate pertinent aspects of the theory and show that (multiple) weak interfaces can be detected and located correctly, with a radial resolution of  $\sim 15$  km for the frequencies used, even in the presence of (random) noise that would prohibit visual inspection and modeling of the subtle signals. We transformed the transverse component  $ScS$  waveforms into image gathers of a CMB patch beneath Central America. Juxtaposition of stacks of these gathers, involving  $\sim 35,000$  seismograms, produces a two-dimensional (2-D) image profile revealing contrasts in elastic properties near the target depth of the CMB and  $\sim 280$ – $340$  km above it. The latter may mark the top of the so called  $D''$  region. The images also reveal a richness of structures in between these depths. Combined with a statistical analysis of these singularities (described in paper 2), the approach to imaging presented here paves the way to large-scale seismic exploration of the lowermost mantle.

**Citation:** Wang, P., M. V. de Hoop, R. D. van der Hilst, P. Ma, and L. Tenorio (2006), Imaging of structure at and near the core mantle boundary using a generalized radon transform: 1. Construction of image gathers, *J. Geophys. Res.*, *111*, B12304, doi:10.1029/2005JB004241.

## 1. Introduction

[2] Earth's large-scale radial stratification was a prime focus of seismology in the first half of the 20th century. In the past decades research emphasis has shifted to mapping the lateral variations in seismic propagation speed and changes in the depth to and character of deep mantle

interfaces and boundary layers associated with thermochemical convection. The relatively smooth variations in seismic wave speed can be delineated by transmission and normal mode tomography [e.g., *Dziewonski*, 1984; *van der Hilst et al.*, 1997; *Romanowicz*, 2003]. Structures at length scales far smaller than can be resolved by tomography cause wavefield scattering, including reflections and phase conversion. Scattering of seismic waves has been used, for instance, to estimate stochastic properties of deep mantle heterogeneity [e.g., *Hedlin et al.*, 1997; *Margerin and Nolet*, 2003], to determine variations in depth to and reflectivity of known mantle discontinuities [e.g., *Paulssen*, 1988; *van der Lee et al.*, 1996; *Shearer and Flanagan*, 1999; *Shearer et al.*, 1999; *Gu and Dziewonski*, 2002; *Deuss and Woodhouse*, 2002; *Chambers et al.*, 2005], to explore the lowermost mantle [e.g., *Garnero*, 2000; *Castle and Creager*, 2000], and to search for previously unknown interfaces

<sup>1</sup>Department of Earth, Atmospheric, and Planetary Sciences, Massachusetts Institute of Technology, Cambridge, Massachusetts, USA.

<sup>2</sup>Center for Computational and Applied Mathematics, Purdue University, West Lafayette, Indiana, USA.

<sup>3</sup>Department of Statistics, University of Illinois, Champaign, Illinois, USA.

<sup>4</sup>Department of Mathematical and Computer Sciences, Colorado School of Mines, Golden, Colorado, USA.

[e.g., *Lay and Helmberger, 1983; Revenaugh and Jordan, 1991; Kawakatsu and Niu, 1994; Vinnik et al., 2001; Castle and van der Hilst, 2003*].

[3] The remote sensing of deep mantle discontinuities and, in particular, the lowermost mantle (that is, the core-mantle boundary (CMB) and  $D''$ ), is a challenge because the seismic waves used to probe them propagate through Earth's heterogeneous shallow mantle before they are observed. Forward modeling of judiciously selected seismological phases has shown convincingly that at and near the CMB strong heterogeneity exists on a wide spectrum of length scales [e.g., *Garnero, 2000; Rost and Revenaugh, 2004; Helmberger and Ni, 2005*]. However, forward modeling of complex waveforms is, as yet, only practical for relatively simple structural geometries, and it requires waveforms in which the signal of interest has sufficient amplitude. The latter often implies a restriction to fairly small epicentral distance ranges, which, in turn, restricts the CMB regions that can be studied. Moreover, one needs to have prior knowledge of the target structures. As a complementary technique, imaging by inversion of seismic data can overcome some of these limitations and can be used to explore "Terra Incognita." Traditional seismic inverse theory, however, allows for the correct interpretation of only a fraction of the information contained in multicomponent broadband waveform data. Moreover, noise from various sources can mask weak signals in the seismic data. Signal can be enhanced by stacking, and in recent years several exciting applications to lowermost mantle imaging have been published [e.g., *Thomas et al., 2004; Hutko et al., 2006; Avants et al., 2006b*]. However, these studies require laborious data analysis (including visual inspection and forward modeling at some stage of the analysis), which complicates application to large data sets and geographical regions.

[4] With the rapidly increasing availability of broadband global network data and data from dense receiver arrays, such as the USArray component of EarthScope, there is a well recognized need for the development of methodologies for automated extraction of structural signal from large data sets. To enable the detection, imaging, and characterization of singularities (including interfaces) using large data volumes, we combine concepts from inverse scattering and modern statistics into a two-step strategy. The first step, presented here, is the development of a generalized radon transform (GRT) of broadband global seismic network data to produce so-called common image point gathers, which reveal and characterize multiscale variations in acoustoelastic properties at and near interfaces. In a companion paper, P. Ma et al. (Imaging of structure at and near the core mantle boundary using a generalized radon transform: 2. Statistical inference of singularities, submitted to *Journal of Geophysical Research*, 2006, hereinafter referred to as paper 2) analyze these gathers using "mixed effects" statistical models. The statistical analysis is used to enhance the images and estimate formal (Bayesian) confidence levels. In our automated imaging of Earth's deep interior, the latter replaces forward modeling of (stacks of) waveforms as the (initial) means for model or image validation.

[5] We develop a GRT for imaging of the lowermost mantle with the broadband wavefield formed by direct ScS and its precursors and coda. In section 2 we develop the

theory underlying the GRT and describe how three-component broadband data can be transformed into image gathers. The GRT was introduced to seismic imaging by *Beylkin [1985]* and *Miller et al. [1987]* but the development followed here builds on generalizations due to de Hoop and collaborators [e.g., *de Hoop et al., 1994; de Hoop and Bleistein, 1997; Burridge et al., 1998*]. In section 3 we use synthetic seismograms to illustrate key aspects and test the performance of our methodology. We show that in principle, the GRT can be used to detect (multiple) deep Earth interfaces and estimate their reflection coefficients. We also analyze how the radial resolution depends on the scattering angle. This dependence, which is shown to be related to what is called the dilation in a wavelet transform, is of key importance for the space-scale characterization of the interface. Furthermore, we demonstrate that the GRT is effective in suppressing (random) noise. Finally, in section 4 we discuss pertinent aspects of the data processing, including the use of principal component analysis (PCA) for identifying and separating the direct and scattered wavefields, and we present preliminary results of our study of a CMB patch beneath Central America.

## 2. Generalized Radon Transform to "Uniform" Common Image Point Gathers

### 2.1. Historical Perspective (Anisotropic Elastic Case)

[6] There have been many publications about high-frequency methods to invert seismic data in acoustic media. These methods date back to *Hagedoorn [1954]*; from a seismic perspective, it has taken 30 years to develop the basic analysis [*Schneider, 1978; Clayton and Stolt, 1981; Stolt and Weglein, 1985; Miller et al., 1987; Schleicher et al., 1993*]. From a mathematical perspective, the analysis started with the reconstruction of the singular component of the medium coefficients in the Born approximation, in the absence of caustics, by *Beylkin [1985]*, using the framework of generalized radon transforms. *Bleistein [1987]* discussed the case of a smooth jump using *Beylkin's* results. The simplest form of an asymptotic inversion procedure, however, is already given by *Norton and Linzer [1981]*.

[7] *Beylkin and Burridge [1990]* discussed the asymptotic imaging of seismic data in the Born approximation in isotropic elastic media, under a no-caustics assumption. The generalized radon transform in anisotropic elastic media was developed by de Hoop and coworkers [*de Hoop et al., 1994; Burridge et al., 1998; de Hoop et al., 1999*]. *de Hoop and Bleistein [1997]* introduced the imaging and inversion in general anisotropic elastic media, using a Kirchhoff-type approximation.

[8] *Guillemin [1985]* discussed the so-called Bolker condition in the context of generalized radon transforms, which ensures invertibility of the modeling or single scattering operator in the least squares sense. *Stolk and de Hoop [2002]* made use of this result in the development and analysis of the generalized radon transform in anisotropic elastic media allowing the presence of caustics; explicit expressions and algorithmic aspects in this case are given by *de Hoop and Brandsberg-Dahl [2000]*. The foundations of the use of the Kirchhoff approximation in the generalized radon transform, in the presence of caustics, were also given by *Stolk and de Hoop [2002]*. An implementation and

application of these results to exploration seismic data is given by *Brandsberg-Dahl et al.* [2003].

[9] In global seismology, applications and adaptations of the no-caustic isotropic elastic generalized radon transform to scattered teleseismic body waves are given by *Bostock et al.* [2001] and *Poppeliers and Pavlis* [2003]. Poststack migration in the context of receiver functions was discussed by *Rydberg and Weber* [2000].

## 2.2. GRT Imaging of Deep Mantle Interfaces

[10] In essence, the GRT enables the transformation of a large number of broadband seismic waveform data into (multiple) images of a singularity in physical medium properties, for instance a deep mantle interface. In order to do so, however, one has to account carefully for (smooth, possibly anisotropic) 3-D wave speed variations in the background medium, geometrical aspects such as the focal depth and the radiation patterns of the earthquakes considered, and the uneven and sparse sampling (that is, acquisition geometry). Moreover, in applications to earthquake data (that is, passive seismics) one has to estimate and remove (for each earthquake) the source signature and (for each receiver) the instrument response.

[11] In the following sections we introduce the notation regarding the sources and receivers, define the ray geometrical aspects, and develop the transform itself. We explain the multiresolution aspects of common image point gathers, and we discuss (anti)aliasing and other issues related to uneven spatial and spectral sampling.

### 2.2.1. Sources and Receivers: Definitions

[12] We consider waveform data from many sources (earthquakes), indicated by superscript  $s$ , recorded at many receivers (seismograph stations), indicated by superscript  $r$ . The stations are not required to be part of a contiguous, geographically restricted array.

[13] The earthquake epicenters are denoted by  $\mathbf{x}^s$ . We assume that the origin times  $t^s$  are reset to zero, and that the earthquake's time-rise function is deconvolved from the data (the related practicalities are discussed in section 4.2). For each earthquake we write the equivalent body force  $f$  as

$$f_j(\mathbf{x}, t) = -M_{ij}\partial_t\delta(\mathbf{x} - \mathbf{x}^s)H(t - t^s), \quad (1)$$

with  $t^s$  set to 0, where  $M_{ij}$  is the moment tensor. Note that we use the subscript summation convention. The receivers, located at  $\mathbf{x}^r$ , record three displacement components  $u_p(\mathbf{x}^s, \mathbf{x}^r, t)$ ,  $p = 1, 2, 3$ , which, after preprocessing, will be used as input in the GRT.

### 2.2.2. Scattering Geometry: Definitions

[14] The geometry considered in transforming seismic data in a heterogeneous, anisotropic elastic medium is illustrated in Figure 1a, where the image point is denoted by  $\mathbf{y} = (y_1, y_2, y_3)$ . The superscripts  $s$  and  $r$  indicate the association with a ray from a source and a receiver, respectively. The "two-way" traveltime for a particular diffraction branch associated with a raypath connecting  $\mathbf{x}^s$  with  $\mathbf{x}^r$  via  $\mathbf{y}$  is denoted by  $T = T(\mathbf{x}^s, \mathbf{x}^r, \mathbf{y})$ .

[15] The slowness vector of the ray connecting  $\mathbf{x}^s$  with  $\mathbf{y}$  (evaluated at  $\mathbf{y}$ ) is given by  $\mathbf{p}^s(\mathbf{y})$ ; in particular,  $\mathbf{p}^s(\mathbf{x}^s)$  indicates the slowness along this ray evaluated at the source. The projection  $\boldsymbol{\pi}^s(\mathbf{x}^s)$  of  $\mathbf{p}^s(\mathbf{x}^s)$  onto Earth's surface is a

horizontal slowness. Furthermore, we introduce the phase direction (that is, a unit vector normal to the wavefront)  $\hat{\mathbf{k}}^s = \mathbf{p}^s/|\mathbf{p}^s|$  and, following the notation by *Červený* [2001], the phase velocity  $V^s = 1/|\mathbf{p}^s|$ . A similar notation is used for the quantities along the ray connecting the image point with the receiver (that is,  $\mathbf{p}^r(\mathbf{y})$ ,  $\mathbf{p}^r(\mathbf{x}^r)$ ,  $\boldsymbol{\pi}^r(\mathbf{x}^r)$ ,  $\hat{\mathbf{k}}^r$ , and  $V^r$ ). With  $\omega$  the angular frequency,  $\omega\boldsymbol{\pi}^s$  and  $\omega\boldsymbol{\pi}^r$  are (horizontal components of) wave vectors. (We note that  $(s, r, t, \omega\boldsymbol{\pi}^s, \omega\boldsymbol{\pi}^r, \omega)$ , that is, space, time, and their Fourier duals, wave vector and frequency, defines a point in data phase space.) Likewise, the polarization vector,  $\mathbf{h}$ , associated with compressional or shear waves, is defined at the source, receiver, and image point.

[16] The quantity that controls image resolution is what we will call the migration slowness vector,  $\mathbf{p}^m(\mathbf{y}) = \mathbf{p}^s(\mathbf{y}) + \mathbf{p}^r(\mathbf{y})$ , with a direction, known as the migration dip in the exploration literature,  $\boldsymbol{\nu}^m(\mathbf{y}) = \mathbf{p}^m(\mathbf{y})/|\mathbf{p}^m(\mathbf{y})|$ . (We note that  $(\mathbf{y}, \mathbf{p}^m(\mathbf{y}))$  defines a point in image phase space.) Together, the migration dip and the phase directions of incoming and scattered rays define the scattering vector

$$\boldsymbol{\psi} = (\hat{\mathbf{k}}^s + \hat{\mathbf{k}}^r) \times \boldsymbol{\nu}^m \quad (2)$$

at image point  $\mathbf{y}$ .

[17] For a traveltime diffraction branch, and away from caustics at  $\mathbf{x}^r$  or  $\mathbf{x}^s$ , the scattering angle  $\theta$  between incoming and scattered rays at  $\mathbf{y}$  is related to the scattering vector as

$$\sin \theta = |\boldsymbol{\psi}|, \quad \theta = \theta(\mathbf{x}^s, \mathbf{x}^r, \mathbf{y}), \quad (3)$$

and the scattering azimuth  $\psi$  is the angular displacement of the scattering vector at  $\mathbf{y}$ ,

$$\psi = \psi(\mathbf{x}^s, \mathbf{x}^r, \mathbf{y}), \quad (4)$$

normalized to one (that is,  $\psi/|\psi|$ ); see, again, Figure 1a.

## 2.3. Map (De)Migration and Isochrons

[18] Map migration describes how the geometry of a (specular) reflection (defined as a combination of source and receiver coordinates, traveltime, and horizontal slownesses) is mapped to the location and orientation of a reflector [see, e.g., *Kleyn*, 1977; *Douma and de Hoop*, 2006]:

$$\Sigma : (\mathbf{x}^s, \mathbf{x}^r, t, \boldsymbol{\pi}^s, \boldsymbol{\pi}^r) \mapsto (\mathbf{y}, \mathbf{p}^m) \quad t = T(\mathbf{x}^s, \mathbf{x}^r, \mathbf{y}). \quad (5)$$

[19] For given  $(\mathbf{x}^s, \mathbf{x}^r, t)$ , the set of equal times  $T(\mathbf{x}^s, \mathbf{x}^r, \mathbf{y}) = t$  defines an isochron. With slownesses  $\boldsymbol{\pi}^s$  and  $\boldsymbol{\pi}^r$ , which can be inferred from the data (for instance from traveltime slopes, polarization analysis, or vespagrams, see *Rost and Thomas* [2002]), the mapping  $\Sigma$  locates  $\mathbf{y}$  on an isochron. If such slowness information is not used, a data point  $(\mathbf{x}^s, \mathbf{x}^r, t)$  smears over an isochron in the interior of the Earth (see Figure 1b). In fact, the impulse response of the kernel of the generalized radon transform (considered as an integral operator) coincides precisely with an isochron.

[20] The use of isochrons for deep Earth imaging is not new. For example, *Lay and Young* [1996] used them in their study of scattering in Earth's lowermost mantle. Isolating a proper time window of the coda wave (such as  $S$  to  $ScS$ ),

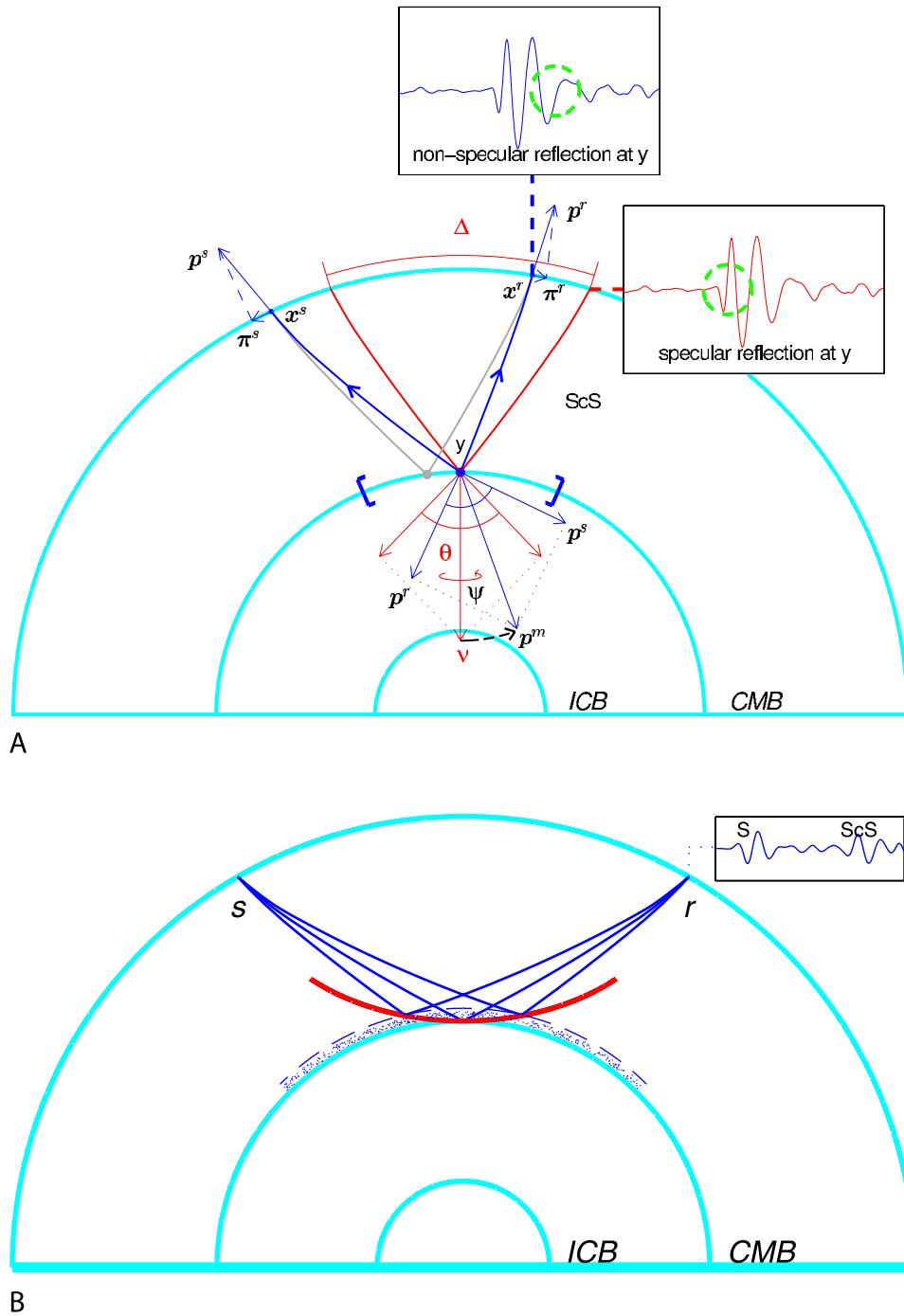


**Figure 1.** Schematic illustration of (a) the path geometry and (b) the isochron concept considered in the generalized radon transform (GRT) of ScS data. In Figure 1a the source ( $\mathbf{x}^s$ ) and receiver ( $\mathbf{x}^r$ ) are separated by epicentral distance  $\Delta$ . The image point at the CMB is denoted  $\mathbf{y}$ . Slowness vectors are given by  $\mathbf{p}$ , and  $\pi$  denote horizontal slownesses. The scattering angle is  $\theta$  and scattering azimuth is  $\psi$ . The image is, essentially, created by integration over  $\mathbf{p}^m$ . All other symbols are defined in the text. The two seismograms illustrate that information about a prescribed image point  $\mathbf{y}$  is gleaned from different parts of data recorded at the different stations; for nonspecular reflections part of the coda contributes to the stacks, whereas for specular reflections the information is retrieved from the main arrival. In Figure 1b, for given  $(\mathbf{x}^s, \mathbf{x}^r, t)$ , the set of points  $\mathbf{y}$  constrained by  $T(\mathbf{x}^s, \mathbf{x}^r, \mathbf{y}) = t$  is identified as an isochron;  $\mathbf{p}^m$  is normal to the isochron.

they applied a convolutional model approach to estimate for any scattered waves the arrival times  $t$  (at a station located at  $\mathbf{x}^r$  for a given earthquake at  $\mathbf{x}^s$ ) and the amplitudes. Thus a combination ( $\mathbf{x}^s$ ,  $\mathbf{x}^r$ ,  $t$ , amplitude) is a data point, and multiple data points smear over a collection of isochrons. Instead of integrating over all isochrons at a particular image point, as done by the generalized radon transform, *Lay and Young* [1996] considered a smooth mantle wave speed model and kept track of how many isochrons associated with their data points hit a particular scattering (image) point in the lower mantle.

#### 2.4. Generalized Radon Transform Inversion

[21] With the geometrical concepts developed above we derive the basic form of the operators that transform the waveform data to a set of common image point gathers in a heterogeneous, anisotropic medium. The elastic properties of the medium under consideration, here Earth's mantle and crust, are described by a stiffness tensor  $c_{ijkl}$  ( $i, j, k, l \in \{1, \dots, 3\}$ ) and mass density  $\rho$ . These parameters are decomposed as a sum of a smooth part (with superscript (0)) and a (nonsmooth) perturbation (superscript (1)):

$$\rho(\mathbf{x}) = \rho^{(0)}(\mathbf{x}) + \rho^{(1)}(\mathbf{x}), \quad c_{ijkl}(\mathbf{x}) = c_{ijkl}^{(0)}(\mathbf{x}) + c_{ijkl}^{(1)}(\mathbf{x}). \quad (6)$$

Accordingly, the (singly scattered) part of the displacement field associated with the perturbed medium properties is denoted with superscript (1), so that  $u = u^{(0)} + u^{(1)}$ . For now we assume that an estimate of the smooth wave speed variations (the background model) is available, for instance from tomography. For a given background model, the medium perturbations, which contain the discontinuities and other types of scatterer, are then found by imaging (or inverse scattering) through application of the GRT.

[22] We further assume that the perturbations are (nonsmooth) changes in elastic parameters across a local, laterally contiguous interface defined by a specific value of some function  $\phi$  [*de Hoop and Bleistein*, 1997]. (Mathematically, the jump function can be readily replaced by an element of a Zygmund class of order between 0 (i.e., a step function) and 1 (i.e., a ramp function), which also determines the local scaling properties of the singularity. This generalization is important, for example, in investigations of phase transitions.) Such a function would describe, for example, the topography of the interface. The interface normal is given by  $\boldsymbol{\nu}_\phi = \nabla\phi/|\nabla\phi|$ . Multiple interfaces are simply treated as a combination of such functions.

[23] We can now formulate the migration of waveform data to uniform image gathers at a pre-described (common) image point  $\mathbf{y}$ . These image gathers will be inferred from  $\hat{S}_w(\mathbf{y}; \theta, \psi)$ , which in turn is obtained from the preprocessed waveform data  $\tilde{u}^{(1)}$  through a GRT of the following form:

$$\hat{S}_w(\mathbf{y}; \theta, \psi) = \int_{E_{\nu^m}} \tilde{u}^{(1)}(\mathbf{x}^s, \mathbf{x}^r, \mathbf{y}) |\mathbf{p}^m(\mathbf{y})|^3 d\nu^m. \quad (7)$$

(This expression is a stripped down version of equation (20) of *Brandsberg-Dahl et al.* [2003]; for instance, the radiation pattern inversion has been removed to enable the direct estimation of a single reflection coefficient instead of multiple combinations of stiffnesses.) As illustrated in

Figure 1, the source and receiver positions are here explicit functions of the image point, migration dip, scatter angle, and azimuth; that is,  $\mathbf{x}^s = \mathbf{x}^s(\mathbf{y}, \nu^m, \theta, \psi)$  and  $\mathbf{x}^r = \mathbf{x}^r(\mathbf{y}, \nu^m, \theta, \psi)$ ; these positions can be determined by ray tracing from image point  $\mathbf{y}$  upward until the rays intersect Earth's surface at the source and receiver side. The integration over migration dip  $\nu^m$  is restricted to  $E_{\nu^m}$ , which depends on  $(\theta, \psi)$  and reflects the effect of the acquisition imprint on the final image. In (7),  $\tilde{u}^{(1)}$  represents the waveform data of the singly scattered constituent  $\tilde{u}_p^{(1)}$  (here ScS and its precursors and coda) corrected for amplitude, polarization, phase, and traveltime at  $\mathbf{y}$  [*Burridge et al.*, 1998, equation (4.2)]:

$$\begin{aligned} \tilde{u}^{(1)}(\mathbf{x}^s, \mathbf{x}^r, \mathbf{y}) = & \overbrace{W(\mathbf{x}^s, \mathbf{x}^r, \mathbf{y})}^{\text{source}} \overbrace{h_p^r(\mathbf{x}^r)}^{\text{polarization}} \overbrace{\partial_t \tilde{u}_p^{(1)}(\mathbf{x}^s, \mathbf{x}^r, T(\mathbf{x}^s, \mathbf{x}^r, \mathbf{y}))}^{\text{waveform data}} \\ & \cdot \underbrace{2 \left[ \rho^{(0)}(\mathbf{x}^r) V^r(\mathbf{x}^r) V^r(\mathbf{y}) V^s(\mathbf{y}) \rho^{(0)}(\mathbf{x}^s) V^s(\mathbf{x}^s) \right]^{1/2}}_{\text{weights related to Green's functions}} \\ & \cdot \underbrace{\left[ \det \mathbf{Q}_2(\mathbf{x}^r, \mathbf{y}) \det \mathbf{Q}_2(\mathbf{y}, \mathbf{x}^s) \right]^{1/2}}_{\text{geometrical spreading}}. \end{aligned} \quad (8)$$

Here, the contraction with  $h_p^r(\mathbf{x}^r)$  represents rotations of the receiver components, and

$$W(\mathbf{x}^s, \mathbf{x}^r, \mathbf{y}) = \frac{1}{2} M_{qr}(\mathbf{x}^s) \left( h_q^s(\mathbf{x}^s) p_r^s(\mathbf{x}^s) + h_r^s(\mathbf{x}^s) p_q^s(\mathbf{x}^s) \right) \quad (9)$$

accounts for the different source mechanisms. Furthermore,  $\tilde{u}_p^{(1)}$  represent the original, singly scattered data  $u_p^{(1)}$  corrected for possible phase shifts due to caustics:

$$\tilde{u}_p^{(1)}(\mathbf{x}^s, \mathbf{x}^r, T(\mathbf{x}^s, \mathbf{x}^r, \mathbf{y})) = \mathcal{H}^{\sigma(\mathbf{x}^r, \mathbf{y}, \mathbf{x}^s)} u_p^{(1)}(\mathbf{x}^s, \mathbf{x}^r, T(\mathbf{x}^s, \mathbf{x}^r, \mathbf{y})), \quad (10)$$

with  $\mathcal{H}$  the Hilbert transform and  $\sigma(\mathbf{x}^r, \mathbf{y}, \mathbf{x}^s) = \kappa(\mathbf{x}^r, \mathbf{y}) + \kappa(\mathbf{y}, \mathbf{x}^s)$  is the accumulated KMAH index [*Červený*, 2001] that keeps track of caustics that occur between  $\mathbf{x}^r$  and  $\mathbf{y}$  and between  $\mathbf{y}$  and  $\mathbf{x}^s$ . Such caustics readily appear in heterogeneous (but smooth) media. Finally,  $\mathbf{Q}_2(\mathbf{x}^r, \mathbf{y})$  and  $\mathbf{Q}_2(\mathbf{y}, \mathbf{x}^s)$  are the relative geometrical spreading [*Červený*, 2001] for the receiver and source rays, respectively. All other parameters are as defined in section 2.2.2.

[24] On the basis of *de Hoop and Bleistein* [1997, equations (37)–(38)] the GRT in (7) is designed to reconstruct a combination of a singular function that characterizes some interface and a smooth (amplitude) function  $S^{(1)}$  that represents the associated scattering coefficient,

$$\underbrace{S^{(1)}(\mathbf{y}; \theta, \psi)}_{\text{smooth amplitude}} \underbrace{(\boldsymbol{\nu}_\phi \cdot \mathbf{p}^m)^{-1} |\nabla_\mathbf{y} \phi| \delta(\phi(\mathbf{y}))}_{\text{interface characterization}}$$

with  $S^{(1)}$  strictly defined only for  $\mathbf{y}$  on the interface defined as a zero level set of a function  $\phi$ ; the normal to the interface at point  $\mathbf{y}$  is given by  $\boldsymbol{\nu}_\phi = \nabla_\mathbf{y} \phi / |\nabla_\mathbf{y} \phi|$ . We note that if the singularity represents a jump (that is, a first-order discontinuity) the scattering coefficient represents the reflection coefficient.

[25] For given  $\mathbf{x}^s$  and  $\mathbf{x}^r$ , let  $\mathbf{x}^\phi$  be the specular reflection point with associated interface dip  $\boldsymbol{\nu}_\phi(\mathbf{x}^\phi)$ . For  $\mathbf{y}$  in the vicinity of this specular reflection point,  $\mathbf{p}^m$  aligns with  $\boldsymbol{\nu}_\phi$ . Using the first-order Taylor expansion of  $\phi(\mathbf{y})$  about  $\mathbf{x}^\phi$  while noting that  $\phi(\mathbf{x}^\phi) = 0$ , that is,  $\phi(\mathbf{y}) \simeq \nabla_{\mathbf{x}}\phi|_{\mathbf{x}^\phi} \cdot (\mathbf{y} - \mathbf{x}^\phi)$ , it follows that the interface characterization can be written as

$$\begin{aligned} (\boldsymbol{\nu}_\phi \cdot \mathbf{p}^m)^{-1} |\nabla_{\mathbf{y}}\phi| \delta(\phi(\mathbf{y})) &\simeq (p^\phi)^{-1} |\nabla_{\mathbf{x}}\phi|_{\mathbf{x}^\phi} \delta(|\nabla_{\mathbf{x}}\phi|_{\mathbf{x}^\phi} \cdot (\mathbf{y} - \mathbf{x}^\phi)) \\ &= (p^\phi)^{-1} \delta(\boldsymbol{\nu}_\phi \cdot (\mathbf{y} - \mathbf{x}^\phi)), \end{aligned}$$

where

$$p^\phi = |\mathbf{p}^m(\mathbf{x}^\phi)|, \text{ such that } \boldsymbol{\nu}^m(\mathbf{x}^\phi) = \boldsymbol{\nu}_\phi(\mathbf{x}^\phi). \quad (11)$$

Using the homogeneity of the delta function (easily checked in its Fourier representation), the interface can then be characterized as

$$(p^\phi)^{-1} \delta(\boldsymbol{\nu}_\phi \cdot (\mathbf{y} - \mathbf{x}^\phi)) = \delta(p^\phi \boldsymbol{\nu}_\phi \cdot (\mathbf{y} - \mathbf{x}^\phi)),$$

and the assumption of a (common) source signature leads to the factorization

$$\hat{S}_w(\mathbf{y}; \theta, \psi) = \hat{S}^{(1)}(\mathbf{x}^\phi; \theta, \psi) w_{(\theta, \psi)}(p^\phi \boldsymbol{\nu}_\phi(\theta, \psi) \cdot (\mathbf{y} - \mathbf{x}^\phi)), \quad (12)$$

for  $\mathbf{y} - \mathbf{x}^\phi$  small, where  $w_{(\theta, \psi)}$  are smooth functions that reveal the imprint at  $\mathbf{x}^\phi$  of the source-receiver distribution [de Hoop and Bleistein, 1997, equation (94)]. We recognize in (12) a dilation (scaling with  $1/p^\phi$ ) and a translation (by  $\mathbf{x}^\phi$ ). Hence, for given direction  $\boldsymbol{\nu}_\phi$ ,  $\hat{S}_w(\mathbf{y}; \theta, \psi)$  behaves like a wavelet transform of the singularity being imaged at  $\mathbf{y}$ . We will see later (section 3) that the dilation plays an important role in characterizing the (radial) scaling properties of the singularities being imaged. In (12),  $\hat{S}^{(1)}(\mathbf{x}^\phi; \theta, \psi)$  denotes the estimate of the scattering coefficient  $S^{(1)}(\mathbf{x}^\phi; \theta, \psi)$  (see Appendix A).

[26] By adjusting the weighting functions inside the integral of (7) we change the GRT given by  $\hat{S}_w(\mathbf{y}; \theta, \psi)$  to a mapping  $\mathcal{I}(\mathbf{y}; \theta, \psi)$  of  $\hat{u}^{(1)}$  to (approximately) uniform image gathers (IGs) in scattering angle  $\theta$  and azimuth  $\psi$  (compare (A4), Appendix A):

$$\mathcal{I}(\mathbf{y}; \theta, \psi) := \int_{E_{\nu, m}} \frac{\tilde{u}^{(1)}(\mathbf{x}^s, \mathbf{x}^r, \mathbf{y})}{W(\mathbf{x}^s, \mathbf{x}^r, \mathbf{y})^2} \frac{|\mathbf{p}^m(\mathbf{y})|^3}{|\mathbf{w}(\mathbf{x}^s, \mathbf{x}^r, \mathbf{y})|} d\nu^m.$$

With this result we derive the structural image through integration over  $\theta$  and  $\psi$ :

$$\mathcal{I}(\mathbf{y}) = \int \int \mathcal{I}(\mathbf{y}; \theta, \psi) d\theta d\psi. \quad (13)$$

In the presence of caustics,  $\mathcal{I}(\mathbf{y}; \theta, \psi)$  commonly generates false image events while the stack  $\mathcal{I}(\mathbf{y})$  over  $(\theta, \psi)$  does not (see Stolk and de Hoop [2005] for details). In paper 2 this linear stack will be replaced by an integration over  $\psi$  followed by formal statistical inference of singularities in the gather.

## 2.5. Sampling

[27] Finally, in the construction and subsequent statistical analysis of the image gathers we have to understand the

effects of sparse and uneven sampling. Typically, the global wavefield is sampled irregularly in  $\mathbf{x}^s$  and  $\mathbf{x}^r$  but regularly in  $t$ . By itself, irregular spatial sampling is an advantage for our approach; in fact, regularly sampled data from regional arrays should be subjected to aliasing tests. Irregular source-receiver sampling obtained by quasi-Monte Carlo sampling of migration dip and scattering angle and azimuth even results in optimal spatial resolution kernels for inverse scattering for a given number of data points [de Hoop and Spencer, 1996].

[28] The sampling properties of the GRT can be described using a table generated by map migration  $\Sigma$  (compare (5))

$$\{(\mathbf{x}^s, \mathbf{x}^r, t, \omega\pi^s, \omega\pi^r, \omega; \mathbf{x}, \omega\mathbf{p}^m) | t = T(\mathbf{x}^s, \mathbf{x}^r, \mathbf{x})\}.$$

The braces, here, indicate that this set of points is a relation; note that, in general, there is not a mapping between  $(\mathbf{x}, \omega\mathbf{p}^m)$  and  $(\mathbf{x}^s, \mathbf{x}^r, t, \omega\pi^s, \omega\pi^r, \omega)$ .

[29] For a given grid, the Fourier duals in this table, that is,  $(\mathbf{x}^s, \omega\pi^s)$ ,  $(\mathbf{x}^r, \omega\pi^r)$ ,  $(t, \omega)$  and  $(\mathbf{x}, \omega\mathbf{p}^m)$ , should satisfy the Nyquist criterion, which essentially provides an upper bound for frequency,  $f_{\max} = \frac{\omega_{\max}}{2\pi}$ . For example, if  $\Delta r$  denotes the (average) station spacing on a gridded array, then

$$f_{\max} |\pi^r| \leq \frac{1}{2\Delta r}.$$

If needed, an antialias filter can be applied. For sampling the image, we note that the magnitude of the (migration) slowness vector is given by

$$|\mathbf{p}^m| = \left[ (V^s)^{-2} + 2(V^s)^{-1}(V^r)^{-1} \cos(\theta) + (V^r)^{-2} \right]^{1/2}, \quad (14)$$

which also shows how  $|\mathbf{p}^m|$  changes with scattering angle  $\theta$ . In practice, spatial aliasing in the image is not an issue because its sampling is part of the (computational) algorithm.

## 3. Resolution Tests With Synthetic Data

[30] We evaluate the performance of the methodology developed above with broadband WKBJ seismograms [Chapman, 1978] calculated from a radially stratified wave speed model (ak135 [Kennett et al., 1995]), on which we superimpose jumps in elastic parameters at certain distances above the CMB. For example, Figure 2a depicts seismograms calculated for a 1.5%  $S$  wave speed contrast at 150 km above the CMB; the records on the right are generated with contrasts at 150, 200, and 250 km above the CMB. Tests such as the ones presented here demonstrate that the GRT can detect small medium contrasts in noise-free data or if the noise in the data is random and white. Other types of noise can degrade the GRT stacks, however, and in paper 2 we assess the performance of the GRT in the presence of nonrandom “noise” (e.g., due to uneven data coverage, errors in the assumed background medium, or multiple scattering) and discuss how the GRT stacks can be enhanced through statistical inference (with mixed effects models).

[31] We consider different geographical source-receiver distributions. In one series of tests we use an idealized

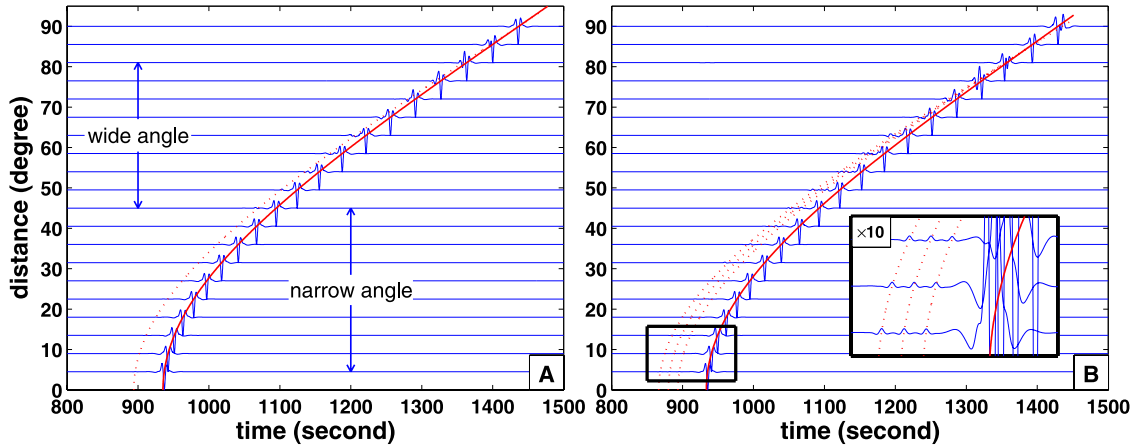


**Figure 2.** Record section of synthetic data for models with (a) one and (b) three contrasts above the CMB, calculated with WKBJ. The red solid lines are the traveltimes curves of *ScS* phase, and the red dotted lines are the traveltimes curves of *SdS* phases. At wide angles this reflection becomes stronger and crosses over with, and eventually arrives in, the coda of direct *ScS*. The inset in Figure 2b shows, for narrow angle reflections, the weak precursory energy (amplified). Narrow angle ( $0-i_i$ ); wide angle ( $i_i-i_c$ ), with  $i_i$  and  $i_c$  the intramission and critical angle, respectively. For the parameters used here,  $i_i = 44.6^\circ$ , and the critical angle for *SdS* is at  $80.6^\circ$ ; the crossover between *SdS* and *ScS* occurs at  $83.5^\circ$ .

geographic distribution of source-receiver pairs (Figures 3a and 3b); in another we use the actual earthquake-station distribution (Figure 3c). We show results for (synthetic) data bandpass filtered between 1 and 10 s.

[32] For the wave speed models and associated ray geometries considered we can calculate the reflection coefficient  $R$  as a function of scatter angle. The theoretical curve (Figure 3b) and the synthetic data (Figure 2b) suggest that three angles are of particular interest.

[33] The intramission angle  $i_i$ , at which no energy is reflected (that is,  $R = 0$ ). In accord with theoretical predictions, Figure 3a shows that the amplitude of *SdS* decreases with increasing opening angle (with  $R < 0$ ) for  $i < i_i$ , becomes zero at  $i = i_i$ , and increases again for  $i > i_i$ , but with opposite polarity (that is,  $R > 0$ ).

[34] The crossover angle  $i_x$ , beyond which *ScS*, the CMB reflection, arrives before *SdS*, the reflection off the shallower interface (which happens because of the imposed increase in wave speed in the lowermost layer).

[35] The critical angle  $i_c$ , beyond which no energy is transmitted into the  $D''$  (head wave). We define narrow angles as  $i$  less than  $i_i$  and wide angles for  $i$  between  $i_i$  and  $i_x$  (or  $i_c$ , if  $i_c < i_x$ ). In Figure 3b we compare the magnitude of the reflection coefficient inferred from the GRT (see Appendix A) and from Snell's law. The inferred reflection coefficient matches the theoretical curve remarkably well, except near and beyond the critical angle (which in this case is  $2 \times \sim 80.6^\circ$ ).

[36] In addition to illustrating how  $i_i$ ,  $i_x$ , and  $i_c$  affect the appearance of the angle gathers, Figures 3a and 3c demonstrates that the width of the reflectors increases (dilates) with increasing scatter angle. This dilation (see (12) and the text following it) depends on  $\theta$  as  $1/\cos(\theta/2)$ . The degradation of radial resolution with increasing distance can be understood from simple ray geometrical considerations: with increasing angle of incidence the vertical slowness decreases and the traveltimes becomes

less sensitive to perturbations in discontinuity depth (in the limit of grazing rays the sensitivity vanishes because at the image point the depth perturbation is perpendicular to the ray). Most forward modeling studies consider (triplicated) waveforms at distances larger than  $\sim 75^\circ$  (which is at the large distance end of what we call wide-angle data) because the *SdS* phase is weak at smaller distances. This leaves a fairly small epicentral distance range that can be used. Moreover, these data have relatively poor resolution to the depth of interfaces. For our purposes, however, the (predictable) variation in depth resolution provides valuable information; indeed, the redundancy contained in the narrow and wide-angle data helps us constrain both the fine-scale and coarser-scale radial variations in elastic properties. This property can be exploited to quantify the space-scale properties of the singularities being imaged.

[37] The ability to reproduce the dilation ( $1/p^\phi$  in (12)) and the reflection coefficients confirms the correct behavior of our GRT. We can also demonstrate that our GRT is able to detect multiple interfaces. For this purpose, we chose 41 imaging points along the great circle transect from ( $-105W, 0$ ) to ( $-75W, 30N$ ). Figure 4 was generated by the lateral juxtaposition of image gathers stacked over wide angles. Using the synthetic data in Figures 2a and 2b, the images depicted in Figures 4a and 4b demonstrate that the CMB and multiple interfaces within  $D''$  are well recovered by the GRT.

[38] Finally, we demonstrate that random noise in the data is suppressed effectively by the GRT. For this test we add noise to data generated from a model with, as before, a CMB and a wave speed increase at 150 km above it (Figure 5). In Figure 5 (top right) we show the image obtained by applying the GRT to the data without noise (shown in Figure 5 (top left)). The CMB as well as the shallower reflector are resolved at depths that correspond to the contrast in wave speed in the background model used.

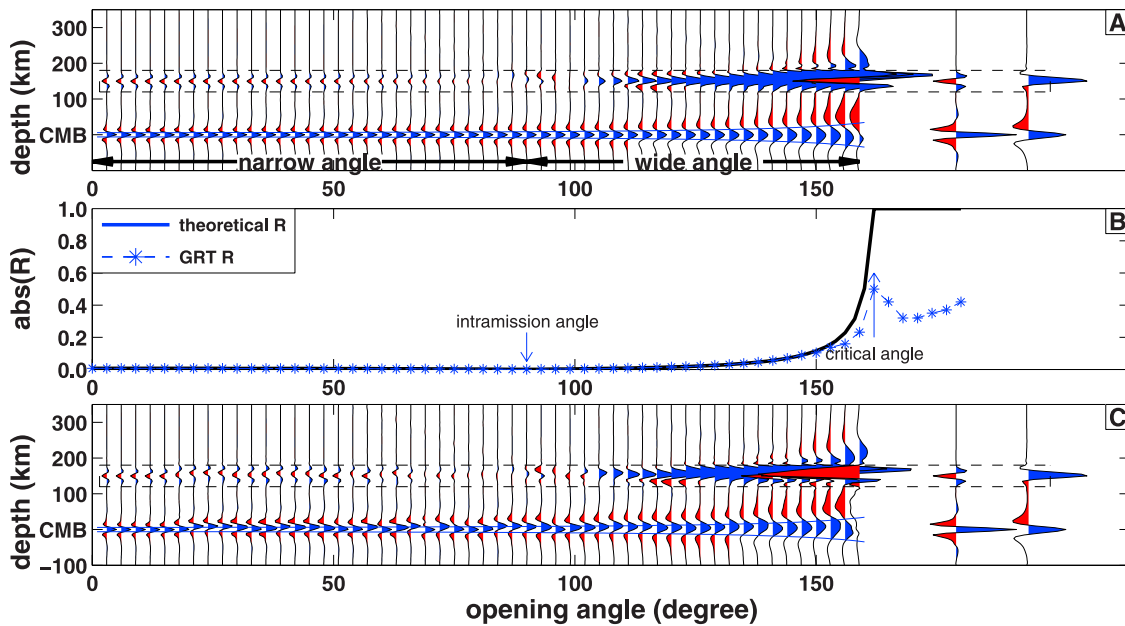


**Figure 3.** Illustration of the construction of GRT stacks (images) from image gathers at different scatter angles. The traces on the left of Figures 3a and 3c are image gathers at 53 scattering angles produced from the synthetic data as in Figure 2. The traces on the right are stacks over narrow and wide angles (as defined in the text and in the caption to Figure 2). We integrate over narrow and wide angles separately because of the change in polarity upon crossing the intramission angle  $i_i$ ; stacking over all angles would involve signals with opposite polarities and could thus mask interfaces. We use a 1–10 s band-pass filter. The gathers and stacks in Figure 3a are produced from an artificial (regular) source-receiver distribution; the results in Figure 3c were computed using the data coverage depicted in Figure 6a. In Figures 3a and 3c the dilation shows up as  $1/\cos(\theta/2)$ ; the theoretical values are depicted by the thin blue lines around the depth of the CMB. To aid visual inspection, the amplitude in the (dashed) box in Figures 3a and 3c is amplified by a factor of 20. In Figure 3b the solid line depicts the reflection coefficient  $R$  calculated from the input model, and the star is the reflection coefficient picked up by our GRT method (see Appendix A). The intramission angle  $i_i = 44.6^\circ$ , and the critical angle  $i_c = 80.6^\circ$ .

Next, we perform the GRT to the data contaminated with noise; the result is shown in Figure 5 (bottom right). The result is practically the same as that of the noise-free data case. Tests like this demonstrate that the GRT is robust

under the addition of white random noise. Even if the signal-to-noise is so low that it is impossible to see the signal from the “top” reflector in the raw data (see inset in Figure 5 (bottom left)), the GRT still yields the contrasts at

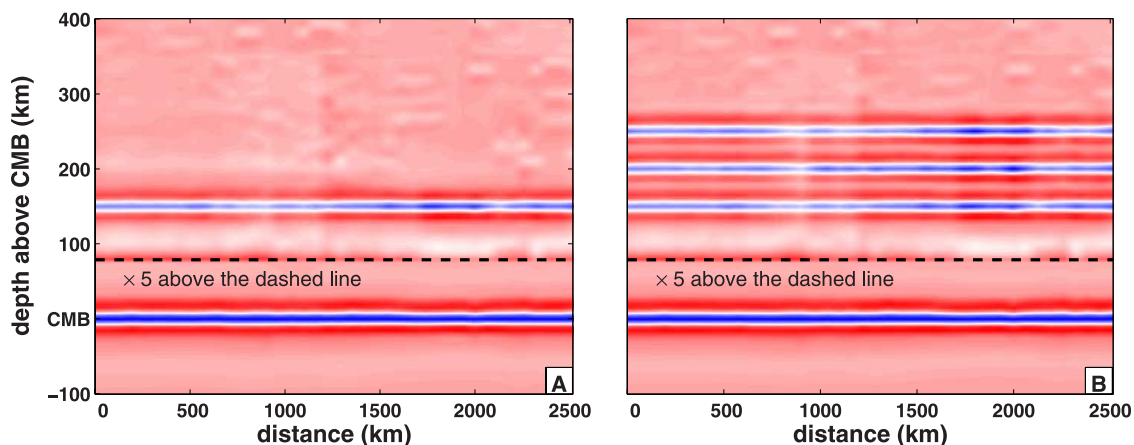


**Figure 4.** Images obtained from narrow angle stacks produced from synthetic data, illustrating the resolution of the GRT. (a) Recovery of the input model with a contrast at 150 km above the CMB. (b) Recovery of the input model with contrasts at 150 km, 200 km, and 250 km above the CMB. The amplitudes above the dashed line are multiplied by a factor of 5 to make them comparable to those of the CMB.

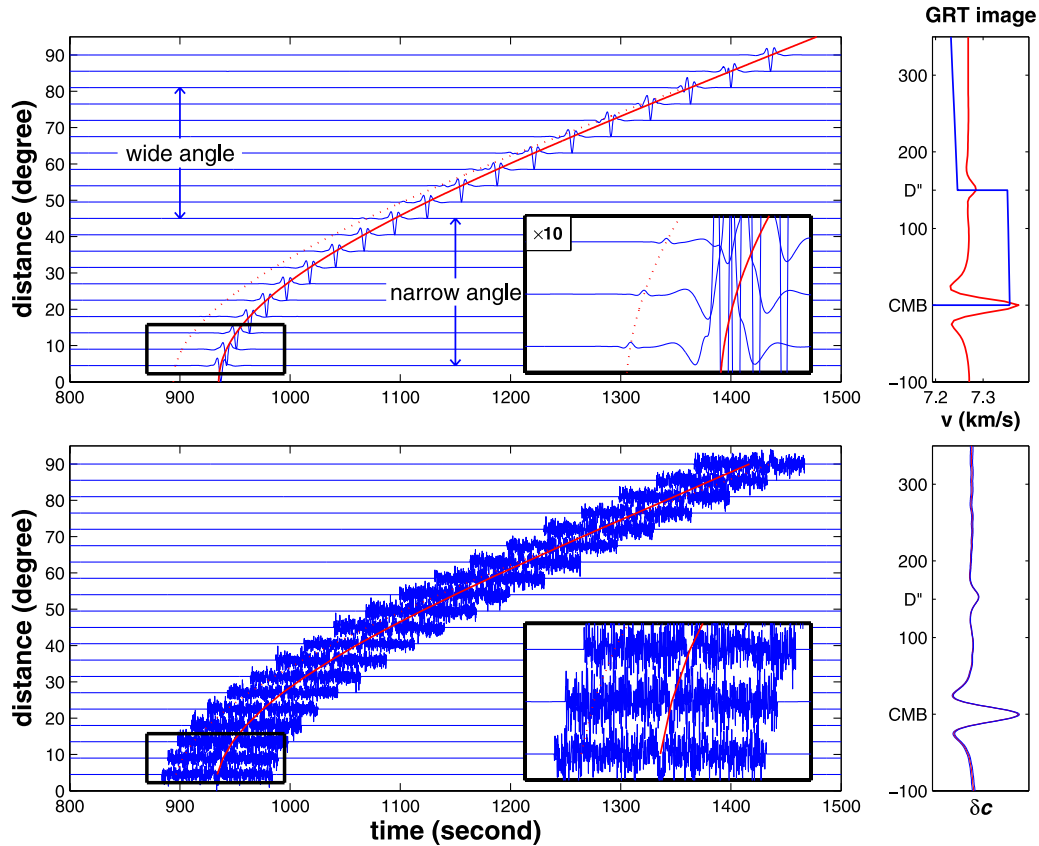


**Figure 5.** Illustration of the robustness of the GRT in the presence of random noise in the data. (top left) Same as Figure 2a. Red lines are theoretical traveltime curves for  $ScS$  (solid) and  $SdS$  (dashed). (top right) GRT image trace (solid red line) constructed from the synthetic data shown on the left and the wave speed profile used to generate the synthetic waveforms (blue curve). (bottom left) Data as in Figure 5 (top) after addition of (random) noise. The arrival of  $ScS$  can still be discerned in the noisy data, but signal from the top reflector has disappeared in the noise. (bottom right) GRT image trace (solid red line) constructed from the noisy data shown on the left. The image is practically identical to the noise-free image.

the right position because it makes use of the redundancy in the data.

#### 4. Imaging the CMB Beneath Central America

[39] We apply the GRT to a broadband wavefield formed by  $ScS$  (and its precursors and coda) that sample a  $50^\circ \times 50^\circ$  core mantle boundary (CMB) beneath Central America (Figure 6a). This region has been studied intensively and several investigators have found evidence for structural complexity within  $D''$  [e.g., *Garnero, 2000; Buffett et al., 2000; Thomas et al., 2004*]. Here we present a sample 2-D image of lowermost mantle structure; a more complete analysis and interpretation of such images is presented in paper 2 and R. van der Hilst et al. (manuscript in preparation, 2006).

##### 4.1. $ScS$ Data Selection and Preprocessing

[40] For all events considered here, origin times and source locations (hypocenters) were obtained from *Engdahl et al. [1998]* and moment tensors and magnitudes from the Harvard centroid moment tensor (CMT) catalog. For all events in our data set, three-component broadband wave-

forms were retrieved from the Data Management Center of the Incorporated Research Institutions for Seismology (IRIS).

[41] The range of epicentral distances that show the most prominent specular  $ScS$  reflections is  $20\text{--}70^\circ$ , but as input to the GRT we used data in the distance range from  $0\text{--}80^\circ$ . We further require that the image points  $y$  are within the CMB patch considered here. The  $\sim 1300$  earthquakes (with  $m_b > 5.2$ , origin times 1988–2002) recorded at one or more of a total of  $\sim 1200$  stations (Figure 6a) yield a total of  $\sim 65,000$  broadband data (Figure 6b). Subsets of this data set are used to construct GRT images at specific CMB locations.

[42] Before we can perform the GRT we subject the data to several preprocessing steps. First, we account (by deconvolution) for the different instrument responses of the seismograph stations from which data are used. Second, we band-passed all data between 1 and 10 s. Third, we remove effects of source and receiver differences on the displacement field  $u$ . To obtain a (common) band-limited source signature, which allows the factorization in (12), we account as well as we can for the differences in rupture mechanisms of all earthquakes

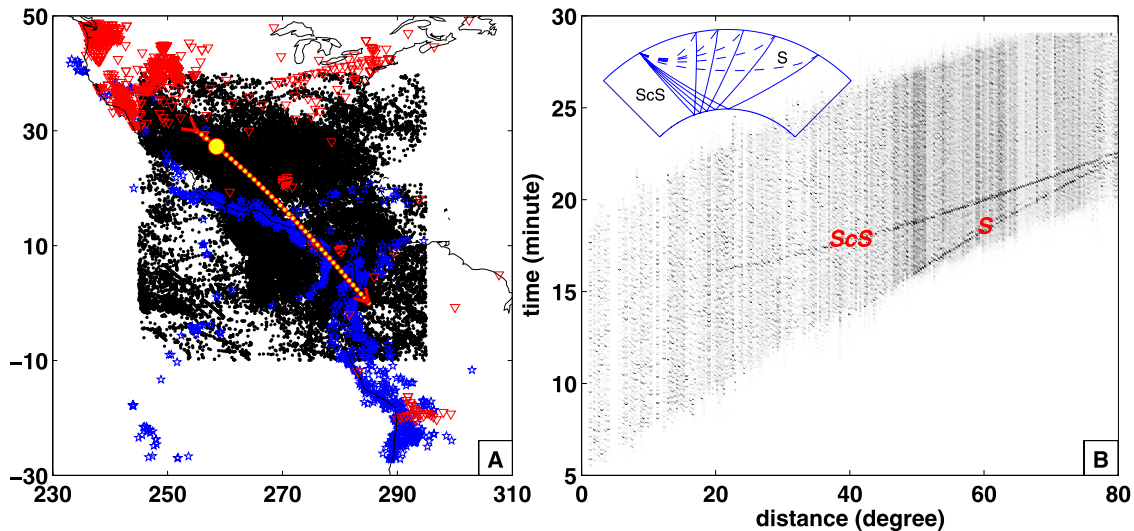


**Figure 6.** (a) Geographic map of the region under study, depicting the epicenters of the  $\sim 1300$  earthquakes (blue stars) and the locations of the  $\sim 1200$  stations (inverted red triangles) that yielded the data used in the construction of the common image point gathers. The  $50^\circ \times 50^\circ$  CMB bin is indicated by the densely sampled rectangle: small black dots mark specular CMB reflection points of the  $\sim 65,000$  ScS data displayed in Figure 6b. The small yellow dots that delineate the NW-SE trending section line mark the locations of the image gathers constituting the 2-D profile presented in Figure 9; the large yellow dot represents the location of the IGs and angle stacks shown in Figure 8. (b) Stack of the  $\sim 65,000$  ScS(SH) data with reflection points in the CMB bin shown in Figure 6a. Processing details data source is IRIS-DMC; band-pass filter is 1–10 s; earthquakes have  $m_b > 5.2$ , with origin time between 1988 and 2002. Inset shows generic ray geometry of ScS. We note that of these data,  $\sim 35,000$  were used for the construction of the 2-D profile shown in Figure 8. (The  $\sim 30,000$  data were rejected either because the specular reflection point was too far from the image points or because the number of seismograms for particular earthquake was inadequate for PCA.)

involved. For this purpose we check the first-onset polarity and deconvolve the time derivative of the source time-rise functions, which can be estimated from CMTs or from a principal component analysis (see section 4.2). Furthermore, all traveltimes are corrected for Earth’s ellipticity [Kennett and Gudmundsson, 1996].

[43] For the CMB bin and the source-receiver pairs considered here, the cone of associated dip directions has an opening of about  $24^\circ$ , which restricts the detectable structural dip angles. (We note that we only consider a cone perpendicular to the CMB, which restricts the structural dip angles; this limitation can be removed by considering multiple cones.) Furthermore, we invoke a bound on the difference between two-way traveltime  $T(\mathbf{x}^s, \mathbf{x}^r, \mathbf{y})$  and the traveltime of the specular reflection at image point  $\mathbf{y}$ . Finally, the broadband seismograms are subjected to windowing in order to obtain time series that comprising main arrivals, their coda, and their precursors.

#### 4.2. Principal Component Analysis (PCA)

[44] As with other techniques involving stacks of earthquake data, we need to account for the differences in source signature of the many different earthquakes involved. Of primary interest here is the source time (rise) function. This can be inferred from the Harvard CMTs, but the frequency content and the type of data

used to obtain the CMT solutions is quite different from those used in our study. Instead of CMTs we use a principal component analysis (PCA) [see, e.g., Rondenay and Fischer, 2003] to estimate the relevant parameters directly from the data. As the direct wavefield we can use either ScS or (teleseismic) S; the latter has the advantage of not being involved in scattering in the CMB region but a disadvantage is that we cannot use some very narrow angles (associated with epicentral distances less than  $30^\circ$ ). The following steps are used to estimate the time-rise functions and to separate the direct and scattered wave fields: (1) The transverse components excited by the same earthquake are divided into different groups according to epicentral distances; if there are fewer than three records in one or more groups, the event (and associated data) is not used; (2) for each group, a Hilbert transform is applied to the seismograms; (3) the transformed seismograms are time normalized using delay times obtained from multichannel cross correlation [e.g., VanDecar and Crosson, 1990]; (4) the seismograms are projected onto the first principal components [see Ulrych et al., 1998], which are determined for each group, and (5) a 100 s window around the calculated traveltime of the direct wave is then used to obtain an empirical “time-rise” function for each record, which is deconvolved from the direct and scattered wavefields to obtain the data used for imaging of the CMB and structure above it, respectively.

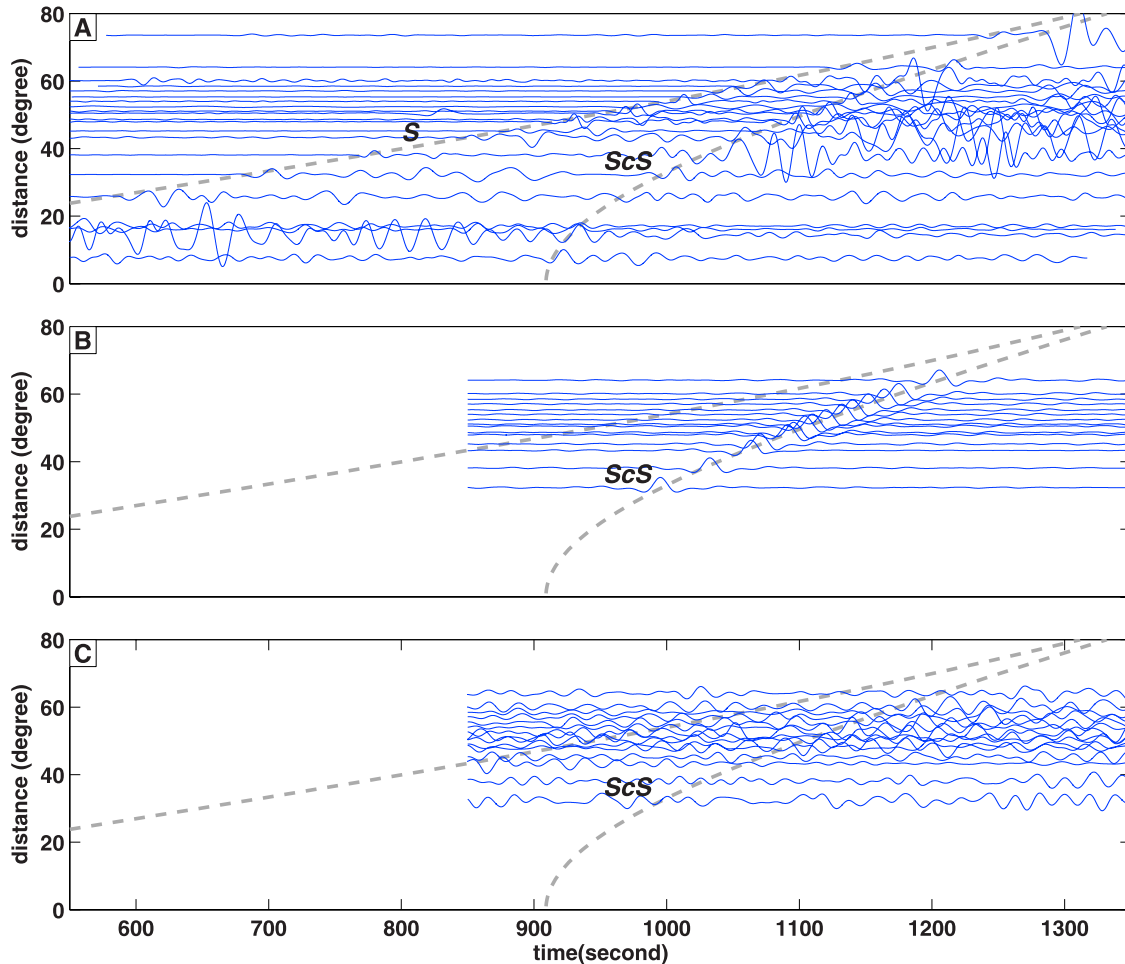


**Figure 7.** Illustration of principal component analysis. (a) (Preprocessed) raw data (see section 4.1). (b) Deconvolution of the raw data using PCA estimation of the derivative of the  $ScS$  time rise function (using a time window of 100 s around  $ScS$ ). (c) Raw data deconvolved with the  $ScS$  estimate minus the field shown in Figure 7b. Traces as in Figures 7b and 7c are used to image the CMB and shallower structure, respectively, as shown in Figure 8a. Similar such estimates based on teleseismic  $S$  as the direct wavefield were used for Figures 8b and 9.

For PCA with  $ScS$  as the reference phase this process is illustrated in Figure 7.

#### 4.3. Preliminary 2-D Image

[45] We draw from the  $\sim 65,000$   $ScS$  displacement records in Figure 6b to construct GRT images of the lowermost beneath Central America (Figure 6a). We first consider an image gather and angle stacks at a particular image point  $\mathbf{y}$  and then construct a 2-D profile by lateral juxtaposition of 41 angle stacks. In the current study we restrict the analysis to the bottom 400 km of the mantle in order to avoid contamination with the  $S$  wavefield.

[46] For  $\mathbf{y}$  at  $(-90^\circ\text{W}, 15^\circ\text{N})$  we integrate over scattering azimuth  $\psi$  and form image gathers for different scattering angles  $\theta$  and hence radial resolution bands (Figure 8). The preliminary results shown here are obtained by integration (according to (13)) either over narrow and wide opening angles, for  $ScS$  as the primary phase (Figure 8a), or over wide angles only, for  $S$  (Figure 8b). We integrate over narrow and wide angles separately because of the change in polarity upon crossing the intramission angle; stacking

over all angles would involve signals with opposite polarities and could thus mask interfaces. The resulting angle stacks are depicted on the right of Figures 8a and 8b. The stacks for either  $ScS$  or  $S$  as the primary phase used in PCA both reveal contrasts in elastic parameters at  $\sim 0$  km (that is, the reference depth of the CMB) and  $\sim 280$ – $340$  km above it. There is also strong evidence for structure in between.

[47] We repeat this procedure to create angle stacks at other image points along a  $\sim 2500$  km long great circle transect from  $(-105^\circ\text{W}, 30^\circ\text{N})$  to  $(-75^\circ\text{W}, 0)$ . Lateral juxtaposition of these stacks creates a (scatter) density plot for the deepest 400 km of Earth's mantle. Of the  $\sim 65,000$  records depicted in Figure 6b,  $\sim 35,000$  were involved in this calculation. The other data were not used either because their specular reflections were too far from the line of section considered or because the number of seismograms for particular earthquake was inadequate for the principal component analysis (see above). The image in Figure 9 shows high scatter from the depth corresponding to the CMB, and it indicates substantial structural complexity in the lowermost mantle above it. In addition to a weakly

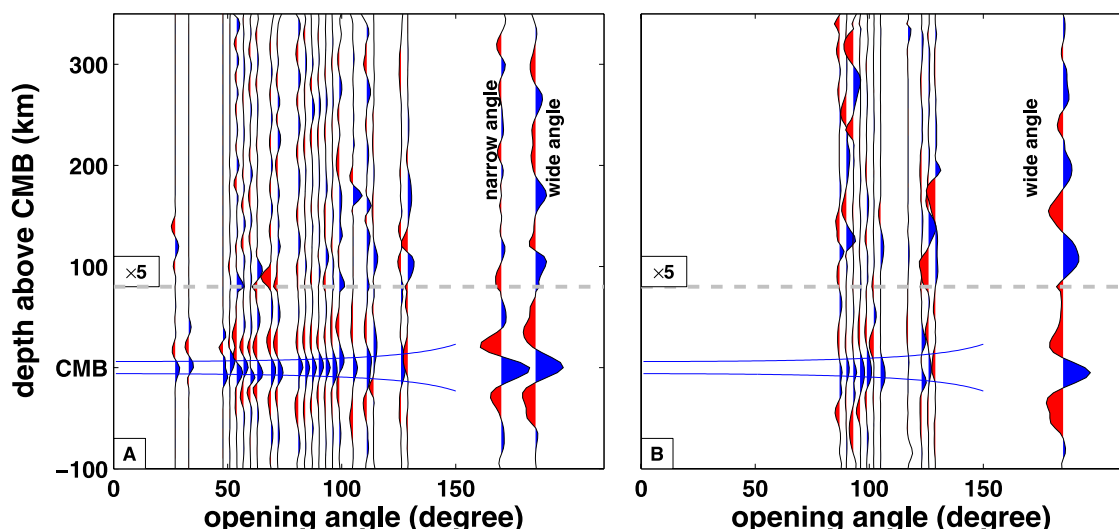


**Figure 8.** Construction of image gathers and angle stacks with real data for an (arbitrary) image point marked by the yellow dot in Figure 6. (a) PCA with *ScS* as the direct wavefield. (b) PCA with (teleseismic) *S*. Similar to Figure 3, in Figures 8a and 8b we show to the right of the image gathers the stacks over the scattering angles. (As before, the theoretical prediction of the dilation is given by the thin blue lines around the depth of the CMB.) Note that for PCA with *S* we only considered wide-angle data.

undulating feature near 280–340 km above CMB, which seems laterally continuous over many hundreds of kilometers, the image reveals pronounced structures at smaller distances above the CMB. We note that these structures are not present in the tests with synthetic data calculated from a single contrast above CMB (e.g., Figure 4).

## 5. Discussion and Concluding Remarks

[48] To enable the efficient exploration of interfaces in Earth's lower mantle over large geographical areas we will combine inverse scattering (through a generalized radon transform) with (mixed effect models) statistical inference and model validation. The generalized radon transform (GRT) of broadband *ScS* data is developed here; the

statistical analysis is presented in paper 2. The GRT method uses three-component, broadband waveforms and exploits the redundancy in large modern data sets. In this context, with redundancy we mean that the combination of specular and nonspecular reflections, at different scattering angles, produce multiple images of the same points in the image. The radial resolution of interface depth depends on (1) the scattering angle (through the dilation, as discussed above and as shown, for instance, in Figure 3) and (2) the frequency of the data used. For periods of  $\sim 5$  s, scatter angles of  $\sim 100^\circ$ , and shear wave speed of  $\sim 8$  km/s, the (quarter wavelength) radial resolution is  $(0.25 \times 5 \times 8) / \cos(100^\circ/2) \sim 15$  km.

[49] In contrast to labor intensive forward modeling of individual or stacked waveforms, our imaging method is

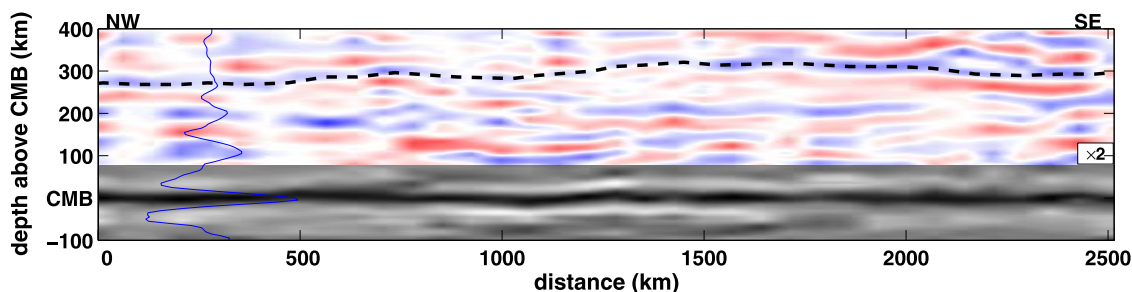


**Figure 9.** A 2-D image of the CMB and lowermost mantle beneath Central America. Using a total of  $\sim 35,000$  broadband records, this 2500 km long profile is produced by juxtaposition of and linear interpolation between angle stacks of the image gathers for 41 image points, evenly spaced along the line of section depicted in Figure 6a. As an example, the stack depicted in Figure 8b is plotted at the NW (that is, left) end of the profile (large yellow dot in Figure 6a). The gray scale part of the image depicts the CMB contrast, whereas the part in color (amplified by a factor of five relative to the CMB part) reveals structure (stratification?) in the lowermost mantle. The dashed line marks the blue contrast (with side lobes in red) at  $\sim 280$ – $340$  km above the CMB, which may represent the top of the so-called  $D''$  region. The image is rich in structure at depths between the CMB and the top of  $D''$ , but we refrain from further interpretation until we have performed a rigorous statistical analysis (paper 2).

highly automated and imposes few a priori constraints on the geometry and nature of the structures that we attempt to image. Indeed, the only prior knowledge concerns the type of seismic phase considered (here, *ScS* and its coda and precursors), so that appropriate time windows can be extracted from the recorded wavefield, and the requirement that (at least locally) the singularities form a contiguous interface. With this information, the data themselves will yield structure in the neighborhood of a predefined imaging point. Since submission of this manuscript, several studies have been published results from Kirchoff migration stacking methods [e.g., *Avants et al.*, 2006a]. Our method has several aspects in common with this technique but differs in that it is explicitly 3-D and that it accounts for wave amplitudes (geometrical spreading and source radiation) and caustics due to wave propagation in a heterogeneous background model. Furthermore, in our automated approach, statistical inference (paper 2) replaces modeling of the (Kirchoff) stacks as the primary means for model validation. Of course, forward modeling can be used to explore in more detail structures of particular interest revealed by our method, but that is beyond the scope of the analysis presented here.

[50] We have performed a series of tests with synthetic data to confirm theoretical predictions, to establish the accuracy of the GRT, and to test the performance of the GRT in the presence of (random) noise. Adding noise to the synthetic data, giving signal-to-noise ratios well below 1, demonstrates that the GRT can detect and locate medium contrasts correctly even if the pertinent signal is not apparent from visual inspection of the “raw” data. With sufficient data coverage, multiple interfaces as well as interfaces marking small medium contrasts (of the order of a few percent) will then be imaged correctly. Sources of error that are not “random” will, however, degrade the GRT images and may increase the minimum medium contrast that can be reliably detected and imaged. Examples of more realistic, nonrandom noise include the distortion of the image gathers due to the uneven source-receiver distribution, the presence of signal due to multiple scattering, and the effects of using an incorrect background wave speed model. In paper 2 we use statistical inference and validation methods to deal with such complications and to quantify the uncertainty of the resulting GRT images. Because this is not done here we will refrain from detailed interpretations of the sample result presented above.

[51] An important aspect, and source of uncertainty, of the GRT presented here as well as similar such methods based (somehow) on the stacking of earthquake data is the estimation and removal (by deconvolution) of the different source pulses. Imperfect removal of the pulse can produce artificial structure in the stacks. *Chambers et al.* [2005] and *Avants et al.* [2006a] visually inspect the deconvolved data and remove bad traces. This labor intensive approach is feasible if one uses “only” several hundred waveforms. For the applications that we are interested in, that is, automated processing of tens or hundreds of thousands of records; this is not feasible and other approaches toward source pulse estimation and deconvolution must be sought. We have considered here a principal component analysis (PCA), but we are exploring the use of more robust (statistical) methods.

[52] We have demonstrated the feasibility of the GRT method with an application to  $\sim 35,000$  broadband records of *ScS* waves that reflect off the CMB beneath Central America. The (preliminary) image profile inferred from these data (Figure 9) reveals strong contrasts in elastic parameters at about 0, that is, at the depth of the CMB. It is encouraging that with neither visual data inspection nor prior assumptions about the geometry of target structures the CMB appears so clearly in the images (e.g., Figures 8 and 9). The 2-D image also reveals a quasi-continuous structure between 280 and 340 km above the CMB. It is tempting to interpret this as the top of the so-called  $D''$  layer. Changes in elastic parameters near this depth have been the subject of many seismological studies [e.g., *Lay and Helmberger*, 1983; *Tromp and Dziewonski*, 1998; *Sidorin et al.*, 1999] (see *Garnero* [2000] for a comprehensive review), but there is as yet no consensus on this transition and its radial and lateral extent. Our preliminary results are consistent with an undulating surfaces [*Thomas et al.*, 2004], but they also reveal structures that could be interpreted as jump-like steps in the discontinuity [*Hutko et al.*, 2006]. Further study is required in order to establish whether such steps are real or whether they can represent a continuous phase boundary (as suggested by *Sun et al.* [2006]) and whether they are a unique, local phenomenon (as implied by *Hutko et al.* [2006]) or a more general feature of  $D''$ .

[53] The image presented here also provides tantalizing evidence for interfaces closer to the CMB. This may suggest that the lowermost mantle is stratified and more complicated than hitherto thought. Further study is needed, however, to establish the (statistical) significance and lateral extent of these multiple transitions. We expect that incorporation of constraints from experimental and theoretical mineral physics with the seismological estimates of interface regularity will help distinguish between compositional, mineralogical, and petrological boundaries. Mineral physicists have recently discovered a phase transformation of  $MgSiO_3$  perovskite at a pressure that could coincide with the contrast depicted between 280 and 340 km above CMB [*Murakami et al.*, 2004; *Shim et al.*, 2004]. It should be noted, however, that important aspects of this purported phase transition remain either unknown or uncertain (D. Shim, Massachusetts Institute of Technology, personal communication, 2005).

[54] In addition to statistical analysis (paper 2) and crosscutting seismology-mineralogy analyses, a logical follow-up of the study presented here would be the exploration of much larger CMB regions. This extension of our current study is possible because of the availability of large volumes of data through international data centers. We note, however, that elsewhere in the world the data coverage may not be as good as considered in the area of interest here, which would make the statistical analysis for image enhancement and validation (paper 2) all the more important.

## Appendix A: Amplitude Analysis of the GRT Image Gathers

[55] In this appendix we discuss an expression for  $S^{(1)}$  by accounting properly for the source and contrast source radiation patterns in modeled seismic data. This also leads to an introduction of residual amplitude compensation

within the GRT, here derived from the Born-Kirchhoff approximation for scattered body waves.

[56] The relative contrast in the medium parameters is formally defined by the “vector”

$$\mathbf{C}^{(1)}(\mathbf{y}) = \left\{ \frac{\rho^{(1)}(\mathbf{y})}{\rho^{(0)}(\mathbf{y})}, \frac{c_{ijkl}^{(1)}(\mathbf{y})}{\rho^{(0)}(\mathbf{y})V_\phi^s(\mathbf{y})V_\phi^r(\mathbf{y})} \right\}^T. \quad (\text{A1})$$

Its dimension (number of independent parameters) depends on the local symmetry of the elastic medium. Here,  $V_\phi^s$  and  $V_\phi^r$  are the phase velocities at  $\mathbf{y}$  averaged over phase angles. We have assumed that  $\mathbf{C}^{(1)}(\mathbf{y}) = \tilde{\mathbf{C}}^{(1)}(\mathbf{y}, \phi(\mathbf{y}))$  with  $(\tilde{\mathbf{C}}^{(1)})'(\mathbf{y}, \phi(\mathbf{y})) = \mathbf{C}(\mathbf{y}) \delta(\phi(\mathbf{y}))$ , where  $\{\}'$  denotes the derivative with respect to the second argument, and  $\mathbf{C}$  denotes the local magnitude of the jump across (a specific value) of the function  $\phi$  that defines the interface. Then (equation (38),(62))

$$S^{(1)}(\mathbf{x}^\phi; \theta, \psi) = W(\mathbf{x}^s, \mathbf{x}^r, \mathbf{x}^\phi)^2 \mathbf{w}^T(\mathbf{x}^s, \mathbf{x}^r, \mathbf{x}^\phi) \mathbf{C}(\mathbf{x}^\phi), \\ \mathbf{x}^{s,r} = \mathbf{x}^{s,r}(\mathbf{x}^\phi, \nu_\phi, \theta, \psi), \quad (\text{A2})$$

where  $\mathbf{w}$  denotes the vector of radiation patterns

$$\mathbf{w}(\mathbf{x}^s, \mathbf{x}^r, \mathbf{y}) = \left\{ h_m^s(\mathbf{y})h_m^r(\mathbf{y}), [h_i^s(\mathbf{y})p_j^s(\mathbf{y})h_k^r(\mathbf{y}) \cdot p_l^r(\mathbf{y})]V_\phi^s(\mathbf{y})V_\phi^r(\mathbf{y}) \right\}^T. \quad (\text{A3})$$

We refer to  $S^{(1)}$  as linearized scattering coefficients;  $\hat{S}^{(1)}$  is a filtered realization of  $S^{(1)}$ , where the filter is determined by the actual illumination. From the expression for  $S^{(1)}$  we may extract the linearized reflection coefficient

$$\frac{S^{(1)}(\mathbf{x}^\phi; \theta, \psi)}{W_2(\mathbf{x}^s, \mathbf{x}^r, \mathbf{x}^\phi)^2} \frac{1}{\left[ V_\phi^s(\mathbf{x}^\phi)V_\phi^r(\mathbf{x}^\phi)^3 \right]^{1/2} (\nu_\phi \cdot \mathbf{p}^m(\mathbf{x}^\phi))^2}.$$

To estimate directly this reflection coefficient we thus replace in the GRT the obliquity factor  $|\mathbf{p}^m(\mathbf{y})|^3$  by  $|\mathbf{p}^m(\mathbf{y})|$ . If, in contrast, we want to relate the image directly to the stiffness perturbation, we have to use another modification of transform (7): Instead of  $\hat{S}_w(\mathbf{y}; \theta, \psi)$  we then define the image gather  $\mathcal{I}(\mathbf{y}; \theta, \psi)$  as

$$\mathcal{I}(\mathbf{y}; \theta, \psi) := \int_{E_{\nu,m}} \frac{\tilde{u}(\mathbf{x}^s, \mathbf{x}^r, \mathbf{y})}{W(\mathbf{x}^s, \mathbf{x}^r, \mathbf{y})^2} \frac{|\mathbf{p}^m(\mathbf{y})|^3}{|\mathbf{w}(\mathbf{x}^s, \mathbf{x}^r, \mathbf{y})|} d\nu^m. \quad (\text{A4})$$

Here,  $|\mathbf{w}(\mathbf{x}^s, \mathbf{x}^r, \mathbf{y})|$  is the Euclidean norm of the vector of radiation patterns. Thus defined,  $\mathcal{I}(\mathbf{y}; \theta, \psi)$  represents a dimensionality preserving transformation of data to a set of images: the common image point gathers (IGs).

[57] At specular reflection points,  $S^{(1)}$  in (A2) gets replaced by

$$\mathbf{e}(\mathbf{x}^\phi; \theta, \psi)^T \mathbf{C}(\mathbf{x}^\phi) \\ \mathbf{e}(\mathbf{x}^\phi; \theta, \psi) = \frac{\mathbf{w}(\mathbf{x}^r(\mathbf{x}^\phi, \nu_\phi, \theta, \psi), \mathbf{x}^\phi, \mathbf{x}^s(\mathbf{x}^\phi, \nu_\phi, \theta, \psi))}{|\mathbf{w}(\mathbf{x}^r(\mathbf{x}^\phi, \nu_\phi, \theta, \psi), \mathbf{x}^\phi, \mathbf{x}^s(\mathbf{x}^\phi, \nu_\phi, \theta, \psi))|}.$$

We anticipate that  $\mathbf{e}$  is only weakly dependent on  $(\theta, \psi)$  so that the image gathers  $\mathcal{I}(\mathbf{y}; \theta, \psi)$  are approximately uniform in  $(\theta, \psi)$ .

[58] **Acknowledgments.** We thank Gary Pavlis, Jesse Lawrence, and Justin Revenaugh (Associate Editor, JGR) for their rigorous and constructive reviews, which helped us improve the manuscript. We acknowledge Stéphane Rondenay (MIT) for suggesting to use the principal component analysis to estimate source parameters from the direct wavefield. This study would not have been possible without the efficient data storage at and retrieval from the Data Management Center of the Incorporated Research Institutions for Seismology (IRIS). The research presented here was funded by the Collaboration in Mathematics and Geosciences program of the U.S. National Science Foundation (grant EAR-0417891).

## References

- Avants, M., T. Lay, and E. J. Garnero (2006a), A new probe of ULVZ S-wave velocity structure: Array stacking of ScS waveforms, *Geophys. Res. Lett.*, *33*, L07314, doi:10.1029/2005GL024989.
- Avants, M., T. Lay, S. A. Russell, and E. J. Garnero (2006b), Shear velocity variation within the  $D''$  region beneath the central Pacific, *J. Geophys. Res.*, *111*, B05305, doi:10.1029/2004JB003270.
- Beylkin, G. (1985), Imaging of discontinuities in the inverse scattering problem by inversion of a causal generalized radon transform, *J. Math. Phys.*, *26*, 99–108.
- Beylkin, G., and R. Burridge (1990), Linearized inverse scattering problems in acoustics and elasticity, *Wave Motion*, *12*, 15–52.
- Bleistein, N. (1987), On imaging of reflectors in the Earth, *Geophysics*, *52*, 931–942.
- Bostock, M., S. Rondenay, and J. Shragge (2001), Multiparameter two-dimensional inversion of scattered teleseismic body waves, *J. Geophys. Res.*, *106*, 30,771–30,782.
- Brandsberg-Dahl, S., M. V. de Hoop, and B. Ursin (2003), Focusing in dip and AVA compensation on scattering-angle/azimuth gathers, *Geophysics*, *68*, 232–254.
- Buffett, B. A., E. J. Garnero, and R. Jeanloz (2000), Sediments at the top of the Earth's core, *Science*, *290*, 1338–1342.
- Burridge, R., M. V. De Hoop, D. Miller, and C. Spencer (1998), Multiparameter inversion in anisotropic media, *Geophys. J. Int.*, *134*, 757–777.
- Castle, J., and K. C. Creager (2000), Local sharpness and shear wave speed jump across the 660-km discontinuity, *J. Geophys. Res.*, *105*(B3), 6191–6200.
- Castle, J. C., and R. D. van der Hilst (2003), Searching for seismic scattering off mantle interfaces between 800 km and 2000 km depth, *J. Geophys. Res.*, *108*(B2), 2095, doi:10.1029/2001JB000286.
- Červený, V. (2001), *Seismic Ray Theory*, Cambridge Univ. Press, New York.
- Chambers, K., J. Woodhouse, and A. Deuss (2005), Topography of the 410-km discontinuity from PP and SS precursors, *Earth Planet. Sci. Lett.*, *235*, 610–622.
- Chapman, C. (1978), New method for computing synthetic seismograms, *Geophys. J. Int.*, *54*, 481–518.
- Clayton, R. W., and R. H. Stolt (1981), A born-wkjb inversion method for acoustic reflection data, *Geophysics*, *46*, 1559–1567.
- de Hoop, M. V., and N. Bleistein (1997), Generalized radon transform inversions for reflectivity in anisotropic elastic media, *Inverse Problems*, *13*, 669–690.
- de Hoop, M. V., and S. Brandsberg-Dahl (2000), Maslov asymptotic extension of generalized radon transform inversion in anisotropic elastic media: A least-squares approach, *Inverse Problems*, *16*, 519–562.
- de Hoop, M. V., and C. Spencer (1996), Quasi Monte-Carlo integration over  $S^2 \times S^2$  for migration  $\times$  inversion, *Inverse Problems*, *12*, 219–239.
- de Hoop, M. V., R. Burridge, C. Spencer, and D. Miller (1994), Generalized radon transform amplitude versus angle (GRT/AVA) migration/inversion in anisotropic media, *Proc SPIE*, *2301*, 15–27.
- de Hoop, M. V., C. Spencer, and R. Burridge (1999), The resolving power of seismic amplitude data: An anisotropic inversion/migration approach, *Geophysics*, *64*, 852–873.
- Deuss, A., and J. H. Woodhouse (2002), A systematic search for mantle discontinuities using SS-precursors, *Geophys. Res. Lett.*, *29*(8), 1249, doi:10.1029/2002GL014768.
- Douma, H., and M. V. de Hoop (2006), Explicit expressions for prestack map time migration in isotropic and VTI media and the applicability of map depth migration in heterogeneous anisotropic media, *Geophysics*, *71*, S13–S28.
- Dziewonski, A. M. (1984), Mapping the lower mantle: Determination of lateral heterogeneity in  $P$  velocity up to degree and order 6, *J. Geophys. Res.*, *89*, 5929–5952.
- Engdahl, E. R., R. D. van der Hilst, and R. P. Buland (1998), Global teleseismic earthquake relocation from improved travel times and procedures for depth determination, *Bull. Seismol. Soc. Am.*, *88*(3), 722–743.
- Garnero, E. J. (2000), Heterogeneity of the lowermost mantle, *Annu. Rev. Earth Planet. Sci.*, *28*, 509–537.

- Gu, Y. J., and A. M. Dziewonski (2002), Global variability of transition zone thickness, *J. Geophys. Res.*, *107*(B7), 2135, doi:10.1029/2001JB000489.
- Guillemin, V. (1985), On some results of Gel'fand in integral geometry, in *Pseudodifferential Operators and Applications (Notre Dame, Ind., 1984)*, pp. 149–155, Am. Math. Soc., Providence, R. I.
- Hagedoorn, J. G. (1954), A process of seismic reflection interpretation, *Geophys. Prospect.*, *2*, 85–127.
- Hedlin, M., P. Shearer, and P. Earle (1997), Seismic evidence for small-scale heterogeneity throughout the Earth's mantle, *Nature*, *387*, 145–150.
- Helmberger, D., and S. Ni (2005), Seismic modeling constraints on the South African superplume, in *Earth's Deep Mantle: Structure, Composition, and Evolution*, *Geophys. Monogr. Ser.*, vol. 160, edited by R. D. van der Hilst et al., pp. 63–82, AGU, Washington, D. C.
- Hutko, A., T. Lay, E. Garnero, and J. Revenaugh (2006), Seismic detection of folded, subducted lithosphere at the core-mantle boundary, *Nature*, *441*, 333–336, doi:10.1038/nature04757.
- Kawakatsu, H., and F. Niu (1994), Seismic evidence for a 920-km discontinuity in the mantle, *Nature*, *371*, 301–305.
- Kennett, B. L. N., and O. Gudmundsson (1996), Ellipticity corrections for seismic phases, *Geophys. J. Int.*, *127*, 40–48.
- Kennett, B., E. Engdahl, and R. Buland (1995), Constraints on seismic velocities in the Earth from travel times, *Geophys. J. Int.*, *122*, 108–124.
- Kleyn, A. (1977), On the migration of reflection time contour maps, *Geophys. Prospect.*, *25*, 125–140.
- Lay, T., and D. Helmberger (1983), A lower mantle S-wave triplication and the shear velocity structure of D'', *Geophys. J. R. Astron. Soc.*, *75*, 799–837.
- Lay, T., and C. J. Young (1996), Imaging scattering structures in the lower mantle by migration of long-period S waves, *J. Geophys. Res.*, *101*(B9), 20,023–20,040.
- Margerin, L., and G. Nolet (2003), Multiple scattering of high-frequency seismic waves in the deep Earth: PKP precursor analysis and inversion for mantle granularity, *J. Geophys. Res.*, *108*(B11), 2514, doi:10.1029/2003JB002455.
- Miller, D., M. Oristaglio, and G. Beylkin (1987), A new slant on seismic imaging: Migration and integral geometry, *Geophysics*, *52*, 943–964.
- Murakami, M., K. Hirose, K. Kawamura, N. Sata, and Y. Ohishi (2004), Post-perovskite phase transition in MgSiO<sub>3</sub>, *Science*, *304*, 855–858, doi:10.1126/science.1095932.
- Norton, S. G., and M. Linzer (1981), Ultrasonic scattering potential imaging in three dimensions: Exact inverse scattering solutions for plane, cylindrical, and spherical apertures, *IEEE Trans. Biomed. Eng.*, *BME-28*, 202–220.
- Paulssen, H. (1988), Evidence for a sharp 670-km discontinuity as inferred from P-to-S converted waves, *J. Geophys. Res.*, *93*, 10,489–10,500.
- Poppeliers, C., and G. L. Pavlis (2003), Three-dimensional, prestack, plane wave migration of teleseismic P-to-S converted phases: 1. Theory, *J. Geophys. Res.*, *108*(B2), 2112, doi:10.1029/2001JB000216.
- Revenaugh, J., and T. Jordan (1991), Mantle layering from ScS reverberations: 2. The transition zone, *J. Geophys. Res.*, *96*, 19,763–19,780.
- Romanowicz, B. (2003), Global mantle tomography: Progress status in the past 10 years, *Annu. Rev. Earth Planet. Sci.*, *31*, 303–328.
- Rondenay, S., and K. M. Fischer (2003), Constraints on localized core-mantle boundary structure from multichannel, broadband SKS coda analysis, *J. Geophys. Res.*, *108*(B11), 2537, doi:10.1029/2003JB002518.
- Rost, S., and J. Revenaugh (2004), Small-scale changes of core-mantle boundary reflectivity studied using core reflected PcP, *Phys. Earth Planet. Inter.*, *145*, 19–36.
- Rost, S., and C. Thomas (2002), Array seismology: Methods and applications, *Rev. Geophys.*, *40*(3), 1008, doi:10.1029/2000RG000100.
- Rydberg, T., and M. Weber (2000), Receiver function array: A reflection seismology approach, *Geophys. J. Int.*, *141*, 1–11.
- Schleicher, J., M. Tygel, and P. Hubral (1993), 3-D true-amplitude finite-offset migration, *Geophysics*, *58*, 1112–1126.
- Schneider, W. A. (1978), Integral formulation for migration in two and three dimensions, *Geophysics*, *43*, 49–76.
- Shearer, P., and M. Flanagan (1999), Seismic velocity and density jumps across the 410- and 660-kilometer discontinuities, *Science*, *285*, 1545–1548.
- Shearer, P., M. Flanagan, and M. Hedlin (1999), Experiments in migration processing of SS precursor data to image upper mantle discontinuity structure, *J. Geophys. Res.*, *104*, 7229–7242.
- Shim, S.-H., T. S. Duffy, R. Jeanloz, and G. Shen (2004), Stability and crystal structure of MgSiO<sub>3</sub> perovskite to the core-mantle boundary, *Geophys. Res. Lett.*, *31*, L10603, doi:10.1029/2004GL019639.
- Sidorin, I., M. Gurnis, and D. V. Helmberger (1999), Evidence for a ubiquitous seismic discontinuity at the base of the mantle, *Science*, *286*, 1326–1331.
- Stolk, C. C., and M. V. de Hoop (2002), Microlocal analysis of seismic inverse scattering in anisotropic, elastic media, *Commun. Pure Appl. Math.*, *55*, 261–301.
- Stolk, C. C., and M. V. de Hoop (2005), Modeling of seismic data in the downward continuation approach, *SIAM J. Appl. Math.*, *65*(4), 1388–1406.
- Stolt, R. H., and A. B. Weglein (1985), Migration and inversion of seismic data, *Geophysics*, *50*, 2456–2472.
- Sun, D., R. A. T.-Song, and D. Helmberger (2006), Complexity of D? in the presence of slab-debris and phase changes, *Geophys. Res. Lett.*, *33*, L12S07, doi:10.1029/2005GL025384.
- Thomas, C., E. J. Garnero, and T. Lay (2004), High-resolution imaging of lowermost mantle structure under the Cocos plate, *J. Geophys. Res.*, *109*, B08307, doi:10.1029/2004JB003013.
- Tromp, J., and A. M. Dziewonski (1998), Geoscience—Two views of the deep mantle, *Science*, *281*, 655–656.
- Ulrych, T., M. Sacchi, and S. Freire (1998), Eigenimage processing of seismic sections, in *Covariance Analysis of Seismic Signal Processing*, *Geophys. Dev. Ser.*, vol. 8, edited by R. L. Kirlin and W. J. Done, pp. 241–274, Soc. of Explor. Geophys., Tulsa, Okla.
- VanDecar, J., and R. Crosson (1990), Determination of teleseismic relative phase arrival times using multi-channel cross-correlation and least squares, *Bull. Seismol. Soc. Am.*, *80*, 150–159.
- van der Hilst, R. D., S. Widiyantoro, and E. R. Engdahl (1997), Evidence for deep mantle circulation from global tomography, *Nature*, *386*, 578–584.
- van der Lee, S., H. Paulssen, and G. Nolet (1996), Variability of P660S phases as a consequence of topography of the 660 km discontinuity, *Phys. Earth Planet. Inter.*, *86*, 147–164.
- Vinnik, L., M. Kato, and H. Kawakatsu (2001), Search for seismic discontinuities in the lower mantle, *Geophys. J. Int.*, *147*, 41–56.

M. V. de Hoop, Center for Computational and Applied Mathematics, Purdue University, 150 N. University Street, West Lafayette, IN 47907, USA. (mdehoop@purdue.edu)

P. Ma, Department of Statistics, University of Illinois Urbana-Champaign, 101 Illini Hall, 725 South Wright Street, Champaign, IL 61820, USA. (pingma@uiuc.edu)

L. Tenorio, Department of Mathematical and Computer Sciences, Colorado School of Mines, Golden, CO 80401, USA. (ltenorio@mines.edu)

R. D. van der Hilst, Department of Earth, Atmospheric, and Planetary Sciences, Massachusetts Institute of Technology, 77 Massachusetts Ave., Room 54-522, Cambridge, MA 02139, USA. (hilst@mit.edu)

P. Wang, Department of Earth, Atmospheric, and Planetary Sciences, Massachusetts Institute of Technology, 77 Massachusetts Ave., Room 54-511 Cambridge, MA 02139, USA. (wangp@mit.edu)